

Kinematics of Crustal Deformation along the Central Himalaya

Yogendra Sharma (✉ yogenmaths2738@gmail.com)

Birla Institute of Technology and Science <https://orcid.org/0000-0003-3324-5816>

Sumanta Pasari

Birla Institute of Technology and Science

Kuo-En Ching

National Cheng Kung University

Research Article

Keywords: Central Himalaya, Bayesian inversion model, GPS velocity, Slip rate, Fault geometry

Posted Date: May 27th, 2021

DOI: <https://doi.org/10.21203/rs.3.rs-528343/v1>

License: © ⓘ This work is licensed under a Creative Commons Attribution 4.0 International License.

[Read Full License](#)

1 **Kinematics of crustal deformation along the central Himalaya**

2
3 **Yogendra Sharma^{*1}, Sumanta Pasaria¹, Kuo-En Ching²**

4
5 **ABSTRACT**

6
7 Using an updated set of GPS surface velocities, the present study provides fault locking behavior and slip rate
8 distribution of the Main Himalayan Thrust (MHT) along the central Himalaya. The two-dimensional velocity field is
9 inverted through Bayesian inversion to estimate fault geometry and kinematic parameters of the MHT along the
10 central Himalaya. The modeling results reveal that: (1) MHT is fully locked in the upper flat (0 – 9 km), partially
11 locked along the mid-crustal ramp (15 – 21 km), and it is creeping in the deeper flat (≥ 21 km); (2) there is an
12 insignificant slip rate of MHT along the locked-to-creeping transition zone, indicating its partially coupled/locked
13 behavior; (3) along the deeper flat of the MHT, the estimated creeping rate is ~ 16.3 mm/yr, ~ 14.7 mm/yr, and
14 ~ 14.3 mm/yr along western, central, and eastern Nepal, respectively; and (4) along the MHT on the upper crust, the
15 modeled locking width turns out to be 97 km, 106 km, and 129 km in the western, central, and eastern Nepal,
16 respectively. In addition, the posterior probability distribution of the locking width exhibits a bimodal Gaussian
17 distribution coinciding with the two ramp geometry of the MHT along the western Nepal. Along the foothills of the
18 Higher Himalaya, the inferred locking line is also aligned to the estimated maximum shear strain concentration and
19 observed seismicity along the central Himalaya. With a general agreement to the previous geodetic results,
20 geological estimates, and background seismicity, our findings provide a promising avenue of the contemporary
21 crustal deformation along the Nepal Himalaya. The estimated inversion results in a Bayesian framework exhibit
22 updated fault kinematics of the MHT and hence provides valuable inputs for seismic hazard assessment along the
23 central Himalaya.

24
25 **KEYWORDS:** Central Himalaya, Bayesian inversion model, GPS velocity, Slip rate, Fault geometry

26
27 * Corresponding author's e-mail address: yogenmaths2738@gmail.com

28 ¹ Birla Institute of Technology and Science Pilani, Pilani Campus, India;

29 ² National Cheng Kung University, Tainan, Taiwan

30 1. INTRODUCTION

31 Analysis of geodetic observations with robust inversion models is essential to determine fault kinematics of the main
32 boundary faults (Dal Zilio et al., 2020). Interseismic locking and slip rate distribution along these fault boundaries
33 vary spatially, highlighting sections of locking, creeping, and transition (Dal Zilio et al., 2020). Along the Himalaya,
34 due to underthrusting of the Indian plate beneath the Tibetan Plateau, large earthquakes have occurred along the
35 locked portion of the Main Himalayan Thrust (MHT) (Bilham et al. 2001). Though several geological and geodetic
36 models have explained rupture propagations of past earthquakes and convergence rates across central Himalaya with
37 better statistical fits to their datasets, the fault geometry, and slip rate distribution along the MHT in central
38 Himalaya is still a topic of debate (Lave and Avouac, 2000; Ader et al., 2012; Wobus et al., 2005; Bilham et al.,
39 1997; Lindsey et al., 2018; Hubbard et al., 2016).

40
41 Great earthquakes along the Himalaya have episodically released the strain energy accumulated in the brittle
42 upper part of the fault plane of the MHT (Avouac, 2003; Mugnier et al., 2013; Jouanne et al., 2017). Some well
43 known great earthquakes, such as 1934 Nepal-Bihar, 1505 western Nepal, and 1100 A.D. earthquakes are inferred to
44 nucleate along the locked-to-creeping transition zone and they have propagated through the mid-crustal ramp,
45 reaching to the surface at Main Frontal Thrust (MFT) (Kumar et al., 2006; Sapkota et al., 2013; Bollinger et al.,
46 2014; Jouanne et al., 2017). In the case of major earthquakes, for example, the 2015 Gorkha earthquake, it occurred
47 in the highly coupled brittle section of MHT and could not reach up to the MFT, indicating that such incomplete
48 rupture will eventually contribute to future great ones (Jouanne et al., 2017; Bilham et al., 2017). Thus modeling of
49 interseismic strain rate distribution and fault kinematics may reveal the level of locking and creeping that could help
50 us to understand the geometry of MHT and the limits of future earthquake propagation (Wallace et al., 2005;
51 Burgmann et al., 2005).

52
53 The central Himalaya ($\sim 80^\circ - 89^\circ$ E to $\sim 26^\circ - 31^\circ$ N) is a classic example of a thrust-fold mountain belt
54 where the convergence between India and Eurasia is purely arc-normal (Robinson, 2008). Most of the convergence
55 in this section of the Himalaya seems to be absorbed by the MHT (Avouac, 2003; Ader et al., 2012). Geodetic
56 observations indicate that the upper brittle part of the MHT is fully coupled (0 – 20 km depth), whereas the deeper
57 ductile section is creeping (Bilham et al., 1997; Bilham et al., 1998; Chen et al., 2004; Ader et al., 2012; Lindsey et
58 al., 2018). Since 1997, various fault locking models have been proposed to estimate fault locking and slip rate of the
59 MHT along the central Himalaya (Bilham et al., 1997; Larson et al., 1999; Burgmann et al., 1999; Chen et al., 2004;
60 Jouanne et al., 1999; Bettinelli et al., 2006; Ader et al., 2012; Stevens and Avouac, 2015; Li et al., 2016; Sreejith et
61 al., 2018; Lindsey et al., 2018; Li et al., 2019). These locking models assume that the MHT is locked from the
62 surface to about 20 km depth. Results in this setup have inferred that the upper crust is locked up to about 100 km
63 width, whereas the deeper portion of the fault plane of the MHT slips with an average rate of ~ 21 mm/yr (Bilham et
64 al., 1997; Bilham et al., 1998; Sreejith et al., 2018; Li et al., 2019; Ader et al., 2012; Larson et al., 1999; Burgmann
65 et al., 1999; Jouanne et al., 1999). Though these models have provided a better understanding of the locking

66 behavior of the upper plate and creeping pattern in the lower edge along the central Himalaya, the transition between
67 the locked zone and the creeping zone is not yet well established.

68

69 In the present study, we utilize an updated set of geodetic measurements from Lindsey et al. (2018) along the
70 central Himalaya. We use a Bayesian fault locking model to estimate the fault kinematics of MHT in the study
71 region comprising six arc-normal transects. We compare the long-term geological slip rates with the geodetic slip
72 rates of the MHT along the central Himalaya. Further, in order to visualize the relationship between observed
73 seismicity and strain rates, we have also computed the geodetic strain rate field along the central Himalaya.

74

75 2. METHODOLOGY

76 To obtain the fault kinematics from the inversion model, we use a recently updated set of GPS surface velocities
77 along the central Himalaya (Fig. 1). The site velocities (in the India-fixed reference frame) are taken from Lindsey et
78 al. (2018). The horizontal velocities are inverted from six along-strike velocity profiles into fault slip rate and other
79 fault geometries (dip angle, rake, locking depth, locking-to-creeping transition zone, fault surface location, locking
80 width) (Fig. 1). In each profile, the relative surface velocity field is computed by fixing the southernmost station.
81 The relative velocity for each profile is decomposed into two components: transect-normal and transect-parallel
82 which account for shortening or lengthening and strike-slip displacement, respectively (Ching et al., 2016).

83 For the inversion, it is assumed that the non-planar fault geometry consists of a basal detachment along
84 with a locked zone, locked-to-creeping transition zone, and creeping zone from the surface trace of MFT to the
85 down-dip end of the MHT (Lindsey et al., 2018). We consider the fault length to be 5000 km so as to minimize the
86 edge effects of the dislocation model (Johnson et al., 2005). To obtain the slip rates using observed geodetic data, we
87 employ the below observation equation:

88

$$d = Gm + \epsilon$$

89

90 Here, G is the function of fault parameters; m is a vector of fault parameters (i.e., dip, slip, length, width,
91 depth, rake, and fault surface location); d is the vector of surface velocities; ϵ represents normally (Gaussian)
92 distributed errors with mean zero and covariance Σ_0 (i.e., $\epsilon \sim N(0, \Sigma_0)$).

93

94 We utilize a Bayesian inversion framework from Fukuda and Johnson (2008) to estimate the fault slip
95 distribution and other fault parameters. In the implementation of the Bayesian inversion, we have used a simple
96 uniform prior (Gaussian distribution of known variance) which depends on the possible range of the model
97 parameters (Bagnardi and Hooper, 2018). Constrained by the geological studies on fault parameters, we define a-
98 priori upper and lower bounds for each parameter, outside of which the prior is considered to be zero (Bagnardi and
99 Hooper, 2018).

100

101 In a Bayesian approach, the posterior distribution (i.e., $P(s, \sigma^2, m|d)$) of unknown parameters is
102 determined from several repetitions of prior information (i.e., $P(s, \sigma^2, m)$) based on how well the parameter
103 knowledge can fit the observed data (likelihood function). Mathematically, the posterior distribution is represented
104 as

$$P(s, \sigma^2, m|d) \propto P(d | s, \sigma^2, m) \times P(s, \sigma^2, m)$$

106
107 The likelihood function ($P(d | s, \sigma^2, m)$), that is defined based on the observed geodetic data for a given
108 fault-slip, follows a Gaussian distribution with mean $G(m) \times s$ and covariance matrix $\sigma^2 \Sigma_0$. To estimate posterior
109 distributions of fault parameters and fault slip, we have employed a Markov Chain Monte Carlo (MCMC) method
110 incorporating the Metropolis algorithm (Fukuda and Johnson, 2008). We have performed 10^6 iterations for each of
111 the parameters in the posterior distribution. Among these iterations, first 'n' (~10% to 20% of the total number of
112 iterations) values that constitute burn-in samples are removed from the final estimation (Bagnardi and Hooper, 2018;
113 Sun et al., 2011; Amey et al., 2018). These 'burn-in' samples comprise primary values, which are often influenced
114 by the initial coarse guesses of the model parameters (Bagnardi and Hooper, 2018; Sun et al., 2011; Amey et al.,
115 2018). More details about the Bayesian inversion approach are available in Fukuda and Johnson (2008).

116 117 3. RESULTS AND DISCUSSION

118 119 3.1 POSTERIOR PROBABILITY DISTRIBUTIONS (PPDS) OF THE FAULT PARAMETERS

120 The advantage of the Bayesian approach in the inversion model over the previous methods (e.g. Bilham et al., 1997;
121 Ader et al., 2012; Stevens and Avouac, 2015; Lindsey et al., 2018) is that the proposed model provides the Posterior
122 Probability Distributions (PPDs) of each fault parameter. The PPDs converge to the best possible solution of fault
123 parameter based on the geodetic observations and upper and lower bounds of parameters (Sun et al., 2011; Bagnardi
124 and Hooper, 2018). The PPDs in the Bayesian approach exhibit a wealth of inferential statistics of the model
125 parameters, such as mean, median, standard deviation, and confidence intervals (Sun et al., 2011; Fukuda and
126 Johnson, 2008; Amey et al., 2018; Bagnardi and Hooper, 2018). The posterior distribution of a fault parameter is
127 expected to follow a Gaussian shape as their mean value converges to the best possible solution of the fault
128 parameter (Sun et al., 2011; Fukuda and Johnson, 2008; Bagnardi and Hooper, 2018). It is observed that in the
129 proposed study, the PPDs for the slip rate and rake angle follow a Gaussian shape in all six profiles. However, the
130 PPDs of some fault parameters (locking depth, locking width, depth of transition zone) show skewed or multi-modal
131 Gaussian distribution (Fig. S1 to Fig. S6). The non-Gaussian distribution might occur due to the a-priori
132 boundedness of these fault parameters. Based on the knowledge of tectonic geometry of the study area, it is
133 reasonable to assume the range of fault geometry as bounded rather than unbounded (Bagnardi and Hooper, 2018).
134 The PPDs for locking width follow bimodal Gaussian shape in C2 and C3 profiles, and in other profiles, they follow
135 Gaussian shape. The PPDs for other parameters, such as locking depth and transition zone depth follow right skewed
136 as well as left-skewed shape, probably due to the boundedness of the a-priori information. The mean values of the

137 model parameters along with their uncertainties (standard deviations) are summarized in [Table 1](#), whereas the PPDs
138 for all parameters are shown in the supplementary figures ([Fig. 4](#) and [Fig. S1-S6](#)).

139

140 **3.2 ESTIMATED LOCKING DEPTH AND LOCKING WIDTH ALONG THE CENTRAL** 141 **HIMALAYA**

142 In the present analysis, we assume that the upper crust is completely locked up to 12 km depth ([Jouanne et al., 2017](#);
143 [Lindsey et al., 2018](#)) ([Fig. 2](#)). Below the locking depth, we consider a locking-to-creeping transition zone varying
144 from 12 km to 22 km depth ([Jouanne et al., 2017](#); [Lindsey et al., 2018](#)) ([Fig. 2](#)). In the deeper part (below the
145 transition zone), the MHT is assumed to be creeping ([Jouanne et al., 2017](#); [Lindsey et al., 2018](#)) ([Fig. 2](#)). Our
146 inversion model suggests that the locking depths along all six profiles vary between 6 km and 9 km ([Fig. 3](#) and
147 [Table 1](#)). Further, we obtain that the locking-to-creeping transition zone lies between 15 km to 21 km depth ([Fig. 3](#)
148 and [Table 1](#)). The upper boundary of the transition zone is assumed to be the down-dip end of the locking depth.
149 Along the central Himalaya, we infer that the obtained transition zone between the locked and creeping portion of
150 the MHT coincides with the belt of the mid-crustal microseismicity underneath the Himalaya ([Fig. 3](#)). This
151 observation agrees with that of [Ader et al. \(2012\)](#). Our estimated range of locked-to-creeping transition zone also
152 coincides with the estimates by [Lindsey et al. \(2018\)](#). The inferred transition zone is one of the important
153 determinants, where future large Himalayan earthquakes might occur ([Bilham et al., 2017](#); [Ader et al., 2012](#)).

154

155 Another important inference from the present study is the locking width, which we have assumed to lie
156 between 80 km and 150 km ([Yin, 2006](#); [Lindsey et al., 2018](#); [Ader et al., 2012](#)). The posterior of locking width in
157 the C2 and C3 profiles reveals a bimodal distribution where the first mode lies between 70 km and 100 km, whereas
158 the second mode lies between 110 km and 130 km ([Fig. 4](#)). The first mode provides a mean value of ~ 85 km,
159 which is located at a distance of about 60 – 70 km in the north direction from the surface trace of the MFT ([Fig. 4](#)).
160 The second mode in the PPDs of locking width ranges between 110 km and 130 km. Both estimates of the locking
161 width in C2 and C3 profiles are located at the same locations where two ramp structure of the MHT in western
162 Nepal has been proposed by several authors ([Harvey et al., 2015](#); [Hubbard et al., 2016](#); [Lindsey et al., 2018](#)) ([Fig. 5](#)).
163 Further, the PPDs of the locking width in C4 to C6 profiles reveal unimodal Gaussian distribution with an average
164 distance of 124 km. Overall, we obtain a heterogeneous locking width along the central Himalaya, which may
165 correspond to the rupture zone of future great Himalayan earthquakes ([Cattin and Avouac, 2000](#); [Burgmann et al.,](#)
166 [2005](#); [Song and Simons, 2003](#); [Wells et al., 2003](#)). It also provides more insight into the geological/rheological
167 properties of the plate interface ([Cattin and Avouac, 2000](#)).

168

169 **3.3 SLIP RATE DISTRIBUTION OF MHT**

170 We have computed the slip rate of the MHT along strike as well as in the down-dip direction across six different
171 profiles. The estimated slip rate along the locked-to-creeping transition zone is 4.4 mm/yr along western Nepal, 5.7
172 mm/yr along central Nepal, and 2.2 mm/yr along eastern Nepal. We infer an insignificant strike-slip component of

173 the total convergence along the central Himalaya probably due to the pure arc-normal convergence of the Indian
174 plate towards the Tibetan Plateau in this region (Ader et al., 2012; Larson et al., 1999; Li et al., 2016; Li et al., 2019;
175 Lindsey et al., 2018). The insignificant strike-slip motion may correspond to a high rake angle of $\sim 98^\circ$ in a pure
176 thrust fault environment along central Nepal (see posterior distributions for the rake parameter in Fig 4). We obtain
177 the lowest dip-slip rate of 12.9 mm/yr in the C3 profile along with 3.5 mm/yr of strike-slip motion along the whole
178 central Himalaya (Fig 3). The low estimated dip-slip rate along the C3 profile may occur due to the north-south
179 trending Thakola rift in the north and Faizabad ridge in the frontal Himalaya (Gahalaut and Kundu, 2012; Dal zilio
180 et al., 2020). The influence of rift and ridge in the low slip rate is also supported by the sparse seismicity along this
181 profile (Fig. 3).

182
183 The total slip rate in the down-dip crust along the MHT is inferred as ~ 16.3 mm/yr, ~ 14.7 mm/yr, and
184 ~ 14.3 mm/yr along western, central, and eastern Nepal, respectively. Though the estimated slip rate of the MHT is
185 generally lower than the slip rate estimates of MHT by Bilham et al. (1997), Chen et al. (2004), Jouanne et al.
186 (2004), Bettinelli et al. (2006), Ader et al. (2012), Stevens and Avouac (2015), and Sreejith et al., (2018), it is
187 consistent with Lindsey et al. (2018). Nonetheless, the small amount of slip accumulation along the transition zone
188 indicates that from the surface to down-dip end, the MHT is segmented into three zones, namely, the fully locked
189 zone ($\sim 0 - 9$ km), locked-to-creeping transition zone or partially locked zone ($\sim 15 - 21$ km), and the fully
190 creeping zone (below ~ 22 km) (Fig. 2).

191 192 **3.4 COMPARISON OF ESTIMATED GEODETIC SLIP RATES AND GEOLOGICAL SLIP** 193 **RATES ALONG THE CENTRAL HIMALAYA**

194 The geological rates are commonly known to reflect the long-term permanent deformation of the crust, whereas the
195 GPS-derived rates include both permanent as well as elastic crustal deformation which eventually gets converted to
196 permanent deformation during future earthquakes (Liu et al., 2000). The geological rates are usually well described
197 by the GPS rates (Nicol and Wallace, 2007), though there are some conflicting findings (Liu et al., 2000). Along the
198 Himalayan arc, most of the geological rates agree within uncertainties to the estimated GPS rates (Lindsey et al.,
199 2018), though the geological studies are confined along the Himalayan front, as trenching in the lower and higher
200 Himalaya is quite difficult. Thus, geological findings are based on the observations along the frontal part of the
201 Himalaya only. In contrast to this, GNSS stations are distributed all over the Himalayan territory, providing better
202 constraints of the present-day surface deformation along the region.

203
204 There are several geological studies as follows. Lave and Avouac (2000) analyzed geomorphic evidence of
205 crustal deformation from terraces of Bagmati and Bakeya rivers along the frontal part of the central Himalaya. They
206 have estimated a long-term slip rate of 21.0 ± 1.5 mm/yr along the MFT. They have suggested that MFT is locked
207 in the interseismic period and will eventually release the accumulated strain through large ($M_w \geq 8.0$) earthquakes
208 in the near future (Lave and Avouac, 2000). Mugnier et al. (2005) studied an uplifted scarp of about 8 m along the
209 MFT in western Nepal. They found that during the Holocene period, the MFT was active with a persistent slip rate

210 of 19 ± 6 mm/yr (Mugnier et al., 2005). Bollinger et al. (2014) studied neotectonic and paleoseismological findings
211 along the MFT in the east-central Himalaya and reported 8.5 – 11.0 mm/yr of slip rate along the MFT. Several
212 geological studies also performed radiocarbon dating of the uplifted scarps during the great historical events along
213 the MFT (Rajendran et al., 2019; Wesnousky et al., 2017). Wesnousky et al. (2017) examined structural and
214 radiocarbon observations of a 11.3 ± 3.5 m dip-slip displacement that occurred due to a great event in 1146 –
215 1256 AD along the MFT and suggested that sufficient strain has been accumulated along the MFT to produce a
216 similar great earthquake with a recurrence interval of ~ 800 years, providing an average 14.1 mm/yr slip rate along
217 the MFT. Rajendran et al. (2019) have reported that the 1505 AD earthquake has produced an average slip of 15 m
218 and will return in about ~ 700 years. This indicates a slip rate of 21.4 mm/yr similar to the MFT slip rate estimate of
219 Lave and Avouac (2000). From the above studies, the average geological slip rate turns out to be 15.8 mm/yr.

220
221 Here we compare the average geological slip rate with the estimated average geodetic slip rate of MHT
222 along the central Himalaya (Liu et al., 2000; Nikolaev, 2002; Zheng et al., 2017; Lindsey et al., 2018). The
223 geological slip of 15.8 mm/yr is comparable to the present geodetic slip rate estimate of 15.1 mm/yr of MHT at a
224 depth of about 22 km. It may be noted that the geological estimates assume slip rate for the entire fault plane,
225 whereas, in the present geodetic fault modeling, we assume that the upper crust is locked (0 – 12 km) as well as
226 partially locked (12 – 22 km). The comparison of geological slip rates with geodetic slip rates indicates that the
227 fault segment of the upper plate (0 – 22 km) is accumulating interseismic slip deficit and will eventually be released
228 in future earthquakes (Zheng et al., 2017).

229 230 **3.5 CORRELATION BETWEEN GEODETIC STRAIN, FAULT LOCKING, AND THE** 231 **BACKGROUND SEISMICITY**

232 The clustering of background seismicity along the central Himalaya, particularly along the front of the Higher
233 Himalaya, closely matches with the down-dip end of the locked fault (Pandey et al., 1995; Cattin and Avouac, 2000;
234 Bollinger et al., 2014; Ader et al., 2012). This correlation indicates that the interseismic strain accumulation at the
235 tip of the creeping zone is possibly responsible for triggering the seismicity in the central Himalaya (Cattin and
236 Avouac, 2000; Bollinger et al., 2014). It may be emphasized that the strain accumulation is not only the responsible
237 parameter in controlling the seismicity, rather the high elevation (≥ 3500 km) and high temperature ($\sim 350^\circ\text{C}$) at
238 the transition zone also affect the releasing of stress build-up and earthquake ruptures (Bollinger et al., 2014;
239 Avouac, 2003; Ader et al., 2012).

240
241 To obtain a geodetic strain rate field along the central Himalaya, we divide the study region into uniform
242 grids ($0.25^\circ \times 0.25^\circ$) and use the surface velocities for estimation of the two-dimensional strain rate field (Shen et
243 al., 1996).

$$W_i = \exp\left(\frac{-d_1^2}{2D^2}\right)$$

245

246 Here W_i is the weighting factor; d_i is the distance between the $i^{\{th\}}$ GPS site and node point; and D is the space
247 of the fourth closest station to the estimating point. The parameter D controls the smoothing of the strain rate field.
248 In the present analysis, based on the resolution of GPS data, the smoothness radius is considered as 80 km which
249 also corresponds to the maximum strain rate variation in the study area.

250

251 Our results (Fig. 5) infer an acceptable correlation between the maximum shear strain rate concentration,
252 northern end of locking width, and Himalayan micro-seismicity belt. Along the central Himalaya, the background
253 seismicity is found to be clustered beneath the Higher Himalaya where the estimated shear strain is concentrated.
254 Large compression rates along the sub-Himalaya and lesser Himalaya indicate that ~ 100 km wide region along the
255 central Himalaya is fully locked and accumulating strain energy for future earthquakes. It is observed that the locked
256 ramp of the MHT along the ~ 110 km length further roots into a sub-horizontal ductile shear zone, where the shear
257 strain rates are higher (Fig. 5). This ductile shear zone along the down-dip flat of the MHT is creeping with a rate of
258 15.1 mm/yr which is comparable with that of the geological estimates during the interseismic period (Lave and
259 Avouac, 2000; Mugnier et al., 2005; Bollinger et al., 2014; Wesnousky et al., 2017; Rajendran et al., 2019).

260

261 4 CONCLUSIONS

262

263 The present study brings out the following conclusions:

- 264 a. The MHT in central Himalaya is found to be locked in the upper flat, partially locked along the mid-crustal
265 ramp, and creeping in the deeper flat.
- 266 b. The creeping rate of the MHT is estimated as ~ 16.3 mm/yr, ~ 14.7 mm/yr, and ~ 14.3 mm/yr along western,
267 central, and eastern Nepal, respectively.
- 268 c. In central and eastern Nepal, an average locking width of 106 km and 129 km is obtained, whereas, in
269 western Nepal, the bimodal distribution of the locking width coincides with the postulated two ramp
270 geometry of the MHT.
- 271 d. The estimated geodetic slip rate of the MHT is comparable to the geological slip rate.
- 272 e. A close correspondence among the maximum shear strain concentration, observed seismicity, and the down-
273 dip end of locked MHT is observed along the central Himalaya.

274 Finally, our proposed locking model resolves fault kinematics of the MHT and provides valuable inputs to
275 contemporary seismic hazard assessment along the central Himalaya.

276

277 ACKNOWLEDGMENTS

278

279 We are thankful to Integrated Research on Disaster Risk, International Center of Excellence (IRDR ICoE-Taipei),
280 Taipei and International Science Council Regional Office for Asia and Pacific (ISC ROAP) for the financial support
281 through seed grant for 2018 TC-EHRA. GMT software was used to prepare some of the figures.
282

283 **COMPETING INTERESTS**

284 The authors declare that they have no competing interests.
285

286 **REFERENCES**

287
288 Ader T, Avouac JP, Liu-Zeng J, Lyon-Caen H, Bollinger L, Galetzka J, Genrich J, Thomas M, Chanard K, Sapkota
289 SN, Rajaure S (2012) Convergence rate across the Nepal Himalaya and interseismic coupling on the Main
290 Himalayan Thrust: Implications for seismic hazard. *J Geophys Res Solid Earth* 117(B4).

291
292 Amey RMJ, Hooper A, Walters RJ (2018) A Bayesian method for incorporating self-similarity into earthquake slip
293 inversions. *J Geophys Res Solid Earth* 123(7), 6052-6071.
294

295 Avouac JP (2003) Mountain building, erosion, and the seismic cycle in the Nepal Himalaya. *Adv Geophys* 46, 1-80.
296

297 Bagnardi M, Hooper A (2018) Inversion of surface deformation data for rapid estimates of source parameters and
298 uncertainties: A Bayesian approach. *Geochem, Geophys, Geosys* 19(7), 2194-2211.
299

300 Bettinelli P, Avouac JP, Flouzat M, Jouanne F, Bollinger L, Willis P, Chitrakar GR (2006) Plate motion of India and
301 interseismic strain in the Nepal Himalaya from GPS and DORIS measurements. *J Geod* 80(8-11), 567-589.
302

303 Bilham R, Larson K, Freymueller J (1997) GPS measurements of present-day convergence across the Nepal
304 Himalaya. *Nat* 386, 61.
305

306 Bilham R, Blume F, Bendick R, Gaur VK (1998) Geodetic constraints on the translation and deformation of India:
307 Implications for future great Himalayan earthquakes. *Cur Sci* 213-229.
308

309 Bilham R, Gaur VK, Molnar P (2001) Himalayan seismic hazard. *Sci* 293(5534), 1442-1444.
310

311 Bilham R, Mencin D, Bendick R, Burgmann R (2017) Implications for elastic energy storage in the Himalaya from
312 the Gorkha 2015 earthquake and other incomplete ruptures of the Main Himalayan Thrust. *Quaternary Int* 462, 3-
313 21.
314

315 Bollinger L, Sapkota SN, Tapponnier P, Klinger Y, Rizza M, Van der Woerd J, Tiwari DR, Pandey R, Bitri A, Bes
316 de Berc S (2014) Estimating the return times of great Himalayan earthquakes in eastern Nepal: Evidence from the
317 Patu and Bardibas strands of the Main Frontal Thrust. *J Geophys Res Solid Earth* 119(9), 7123-7163.
318

319 Burgmann R, Larson KM, Bilham R (1999) Model inversion of GPS and leveling measurements across the
320 Himalaya: Implications of earthquake hazards and geodetic networks. *Himalayan Geol* 20, 59-72.
321

322 Burgmann R, Kogan MG, Steblov GM, Hilley G, Levin VE, Apel E (2005) Interseismic coupling and asperity
323 distribution along the Kamchatka subduction zone. *J Geophys Res Solid Earth* 110(B7).
324

325 Cattin R, Avouac JP (2000) Modeling mountain building and the seismic cycle in the Himalaya of Nepal. *J Geophys*
326 *Res Solid Earth* 105(B6), 13389-13407.
327

328 Chen Q, Freymueller JT, Yang Z, Xu C, Jiang W, Wang Q, Liu J (2004) Spatially variable extension in southern
329 Tibet based on GPS measurements. *J Geophys Res Solid Earth* 109(B9).
330

331 Ching KE, Gourley JR, Lee YH, Hsu SC, Chen KH, Chen CL (2016) Rapid deformation rates due to development
332 of diapiric anticline in southwestern Taiwan from geodetic observations. *Tectonophys* 692, 241-251.
333

334 Dal Zilio L, Jolivet R, van Dinther Y (2020) Segmentation of the Main Himalayan Thrust illuminated by Bayesian
335 inference of interseismic coupling. *Geophys Res Let* 47(4), e2019GL086424.
336

337 Fukuda JI, Johnson KM (2008) A fully Bayesian inversion for spatial distribution of fault slip with objective
338 smoothing. *Bull Seismolo Soci America* 98(3), 1128-1146.
339

340 Gahalaut VK, Kundu B (2012) Possible influence of subducting ridges on the Himalayan arc and on the ruptures of
341 great and major Himalayan earthquakes. *Gondwana Res* 21(4), 1080-1088.
342

343 Harvey JE, Burbank DW, Bookhagen B (2015) Along-strike changes in Himalayan thrust geometry: Topographic
344 and tectonic discontinuities in western Nepal. *Lithosphere* 7(5), 511-518.
345

346 Hubbard J, Almeida R, Foster A, Sapkota SN, Burgi P, Tapponnier P (2016) Structural segmentation controlled the
347 2015 Mw 7.8 Gorkha earthquake rupture in Nepal. *Geolo* 44(8), 639-642.
348

349 Hsu YJ, Simons M, Yu SB, Kuo LC, Chen HY (2003) A two-dimensional dislocation model for interseismic
350 deformation of the Taiwan mountain belt. *Earth Planetary Sci Let* 211(3-4), 287-94.
351

352 Johnson KM, Segall P, Yu SB (2005) A viscoelastic earthquake cycle model for Taiwan. *J Geophys Res Solid Earth*
353 110(B10).
354

355 Jouanne F, Mugnier JL, Pandey MR, Gamond JF, Le Fort P, Serrurier L, Vigny C, Avouac JP (1999) Oblique
356 convergence in the Himalayas of western Nepal deduced from preliminary results of GPS measurements. *Geophys*
357 *Res Let* 26(13), 1933-1936.
358

359 Jouanne F, Mugnier JL, Gamond JF, Le Fort P, Pandey MR, Bollinger L, Flouzat M, Avouac JP (2004) Current
360 shortening across the Himalayas of Nepal. *Geophys J Int* 157(1), 1-4.
361

362 Jouanne F, Mugnier JL, Sapkota SN, Bascou P, Pecher A (2017) Estimation of coupling along the Main Himalayan
363 Thrust in the central Himalaya. *J Asian Earth Sci* 133, 62-71.
364

365 Kumar P, Yuan X, Kind R, Ni J (2006) Imaging the colliding Indian and Asian lithospheric plates beneath Tibet. *J*
366 *Geophys Res Solid Earth* 111(B6).
367

368 Larson KM, Burgmann R, Bilham R, Freymueller JT (1999) Kinematics of the India-Eurasia collision zone from
369 GPS measurements. *J Geophys Res Solid Earth* 104(B1), 1077-1093.
370

371 Lave J, Avouac JP (2000) Active folding of fluvial terraces across the Siwaliks Hills, Himalayas of central Nepal. *J*
372 *Geophys Res Solid Earth* 105(B3), 5735-5770.
373

374 Li Y, Song X, Shan X, Qu C, Wang Z (2016) Locking degree and slip rate deficit distribution on MHT fault before
375 2015 Nepal Mw 7.9 earthquake. *J Asian Earth Sci* 119, 78-86.
376

377 Li S, Wang Q, Chen G, He P, Ding K, Chen Y, Zou R (2019) Interseismic Coupling in the Central Nepalese
378 Himalaya: Spatial Correlation with the 2015 Mw 7.9 Gorkha Earthquake. *Pur Appl Geophys* 176(9), 3893-3911.
379

380 Lindsey EO, Almeida R, Mallick R, Hubbard J, Bradley K, Tsang LL, Liu Y, Burgmann R, Hill EM (2018)
381 Structural control on downdip locking extent of the Himalayan megathrust. *J Geophys Res Solid Earth* 123(6),
382 5265-5278.
383

384 Liu M, Yang Y, Stein S, Zhu Y, Engeln J (2000) Crustal shortening in the Andes: Why do GPS rates differ from
385 geological rates?. *Geophys Res Let* 27(18), 3005-3008.
386

387 Mugnier JL, Huyghe P, Gajurel AP, Becel D (2005) Frontal and piggy-back seismic ruptures in the external thrust
388 belt of western Nepal. *J Asian Ear Sci* 25(5) 707-717.

389
390 Mugnier JL, Gajurel A, Huyghe P, Jayangondaperumal R, Jouanne F, Upreti B (2013) Structural interpretation of
391 the great earthquakes of the last millennium in the central Himalaya. *Ear Sci Rev* 127, 30-47.
392
393 Nicol A, Wallace LM (2007) Temporal stability of deformation rates: Comparison of geological and geodetic
394 observations, Hikurangi subduction margin, New Zealand. *Ear Planet Sci Let* 258(3-4), 397-413.
395
396 Nikolaev VG (2002) Afghan-Tajik depression: Architecture of sedimentary cover and evolution. *Russ J Ear Sci*
397 4(6).
398
399 Pandey MR, Tandukar RP, Avouac JP, Lave J, Massot JP (1995) Interseismic strain accumulation on the Himalayan
400 crustal ramp (Nepal). *Geophys Res Let* 22(7) 751-754.
401
402 Rajendran CP, Sanwal J, John B, Anandasabari K, Rajendran K, Kumar P, Jaiswal M, Chopra S (2019) Footprints of
403 an elusive mid-14th century earthquake in the central Himalaya: Consilience of evidence from Nepal and India.
404 *Geolo J* 54(5), 2829-2846.
405
406 Robinson DM (2008) Forward modeling the kinematic sequence of the central Himalayan thrust belt, western Nepal
407 Himalayan thrust belt, western Nepal. *Geosph* 4(5), 785-801.
408
409 Sapkota SN, Bollinger L, Klinger Y, Tapponnier P, Gaudemer Y, Tiwari D (2013) Primary surface ruptures of the
410 great Himalayan earthquakes in 1934 and 1255. *Nat Geosci* 6(1), 71-76.
411
412 Shen ZK, Jackson DD, Ge BX (1996) Crustal deformation across and beyond the Los Angeles basin from geodetic
413 measurements. *J Geophys Solid Earth* 101(B12) 27957-27980.
414
415 Song TR, Simons M (2003) Large trench-parallel gravity variations predict seismogenic behavior in subduction
416 zones. *Sci* 301(5633), 630-633.
417
418 Sreejith KM, Sunil PS, Agrawal R, Saji AP, Rajawat AS, Ramesh DS (2018) Audit of stored strain energy and
419 extent of future earthquake rupture in central Himalaya. *Scient Rep* 8(1), 1-9.
420
421 Stevens VL, Avouac JP (2015) Interseismic coupling on the main Himalayan thrust. *Geophys Res Let* 42(14), 5828-
422 5837.
423

424 Sun J, Johnson KM, Cao Z, Shen Z, Burgmann R, Xu X (2011) Mechanical constraints on inversion of coseismic
425 geodetic data for fault slip and geometry: Example from InSAR observation of the 6 October 2008 Mw 6.3
426 Daxiang-Yangyi (Tibet) earthquake. *J Geophys Res Solid Earth* 116(B1).
427
428 Wallace K, Bilham R, Blume F, Gaur VK, Gahalaut V (2005) Surface deformation in the region of the 1905 Kangra
429 Mw=7.8 earthquake in the period 1846-2001. *Geophys Res Let* 32(15).
430
431 Wells RE, Blakely RJ, Sugiyama Y, Scholl DW, Dinterman PA (2003) Basin-centered asperities in great subduction
432 zone earthquakes: A link between slip, subsidence, and subduction erosion?. *J Geophys Res Solid Earth* 108(B10).
433
434 Wesnousky SG, Kumahara Y, Chamlagain D, Pierce IK, Reedy T, Angster SJ, Giri B (2017) Large paleoearthquake
435 timing and displacement near Damak in eastern Nepal on the Himalayan Frontal Thrust. *Geophys Res Let* 44(16),
436 8219-8226.
437
438 Wobus C, Heimsath A, Whipple K, Hodges K (2005) Active out-of-sequence thrust faulting in the central Nepalese
439 Himalaya. *Nat* 434(7036), 1008-1011.
440
441 Yin A (2006) Cenozoic tectonic evolution of the Himalayan orogen as constrained by along-strike variation of
442 structural geometry, exhumation history, and foreland sedimentation. *Ear-Sci Rev* 76(1-2), 1-31.
443
444 Zheng G, Wang H, Wright TJ, Lou Y, Zhang R, Zhang W, Shi C, Huang J, Wei N (2017) Crustal deformation in
445 the India-Eurasia collision zone from 25 years of GPS measurements. *J Geophys Res Solid Earth* 122(11), 9290-
446 9312.

Figures

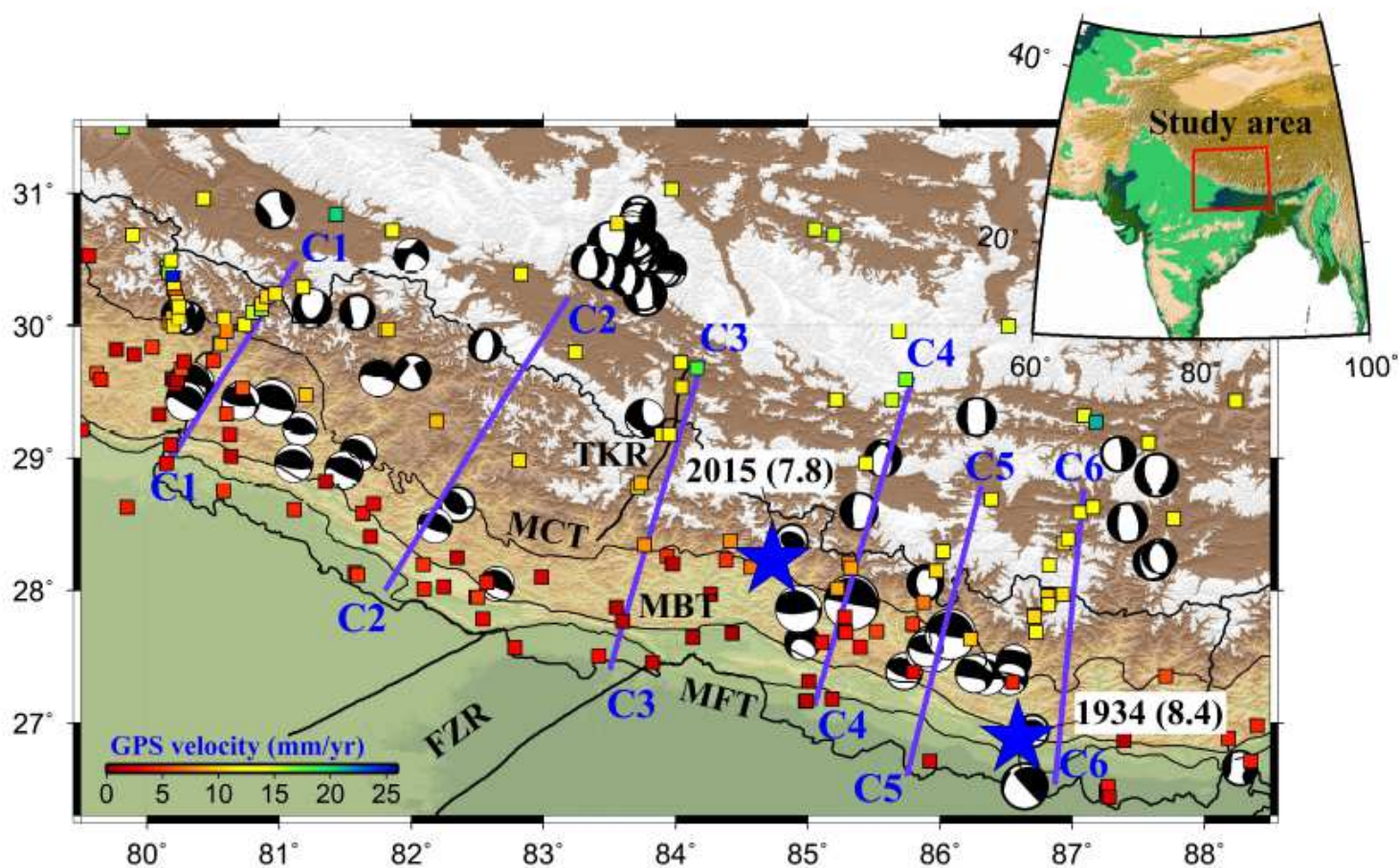


Figure 1

Seismotectonic map of the central Himalaya. Squares represent the GPS surface velocity in the India-Fixed reference frame. Six blue lines are the arc-normal profiles. Focal mechanism solutions of the past earthquakes (since 1976) are represented by the beach balls. MCT: Main Central Thrust, MBT: Main Boundary Thrust, MFT: Main Frontal Thrust, FZR: Faizabad Ridge, and TKR: Thakola Rift. Note: The designations employed and the presentation of the material on this map do not imply the expression of any opinion whatsoever on the part of Research Square concerning the legal status of any country, territory, city or area or of its authorities, or concerning the delimitation of its frontiers or boundaries. This map has been provided by the authors.

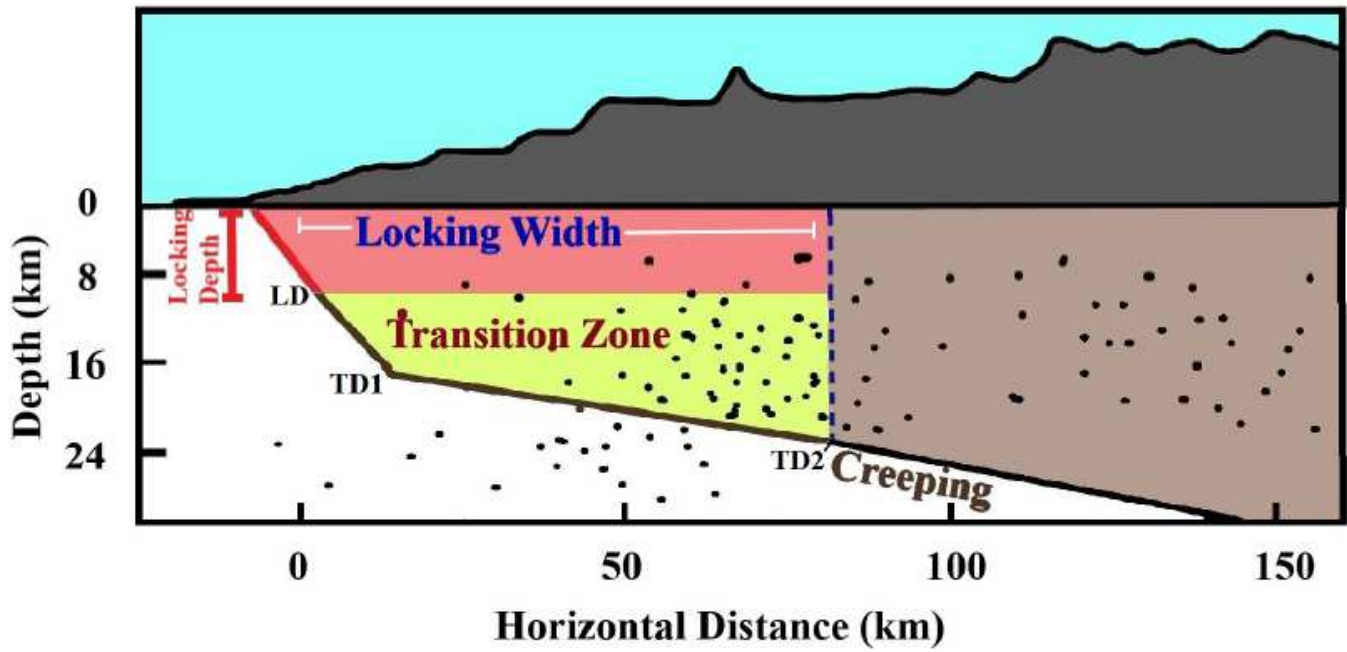


Figure 2

Sketched map of the studied single-fault model. LD: Locking Depth, TD1: Transition zone Depth 1, TD2: Transition zone Depth 2. Small black circles are the representation of the background seismicity along the central Nepal.

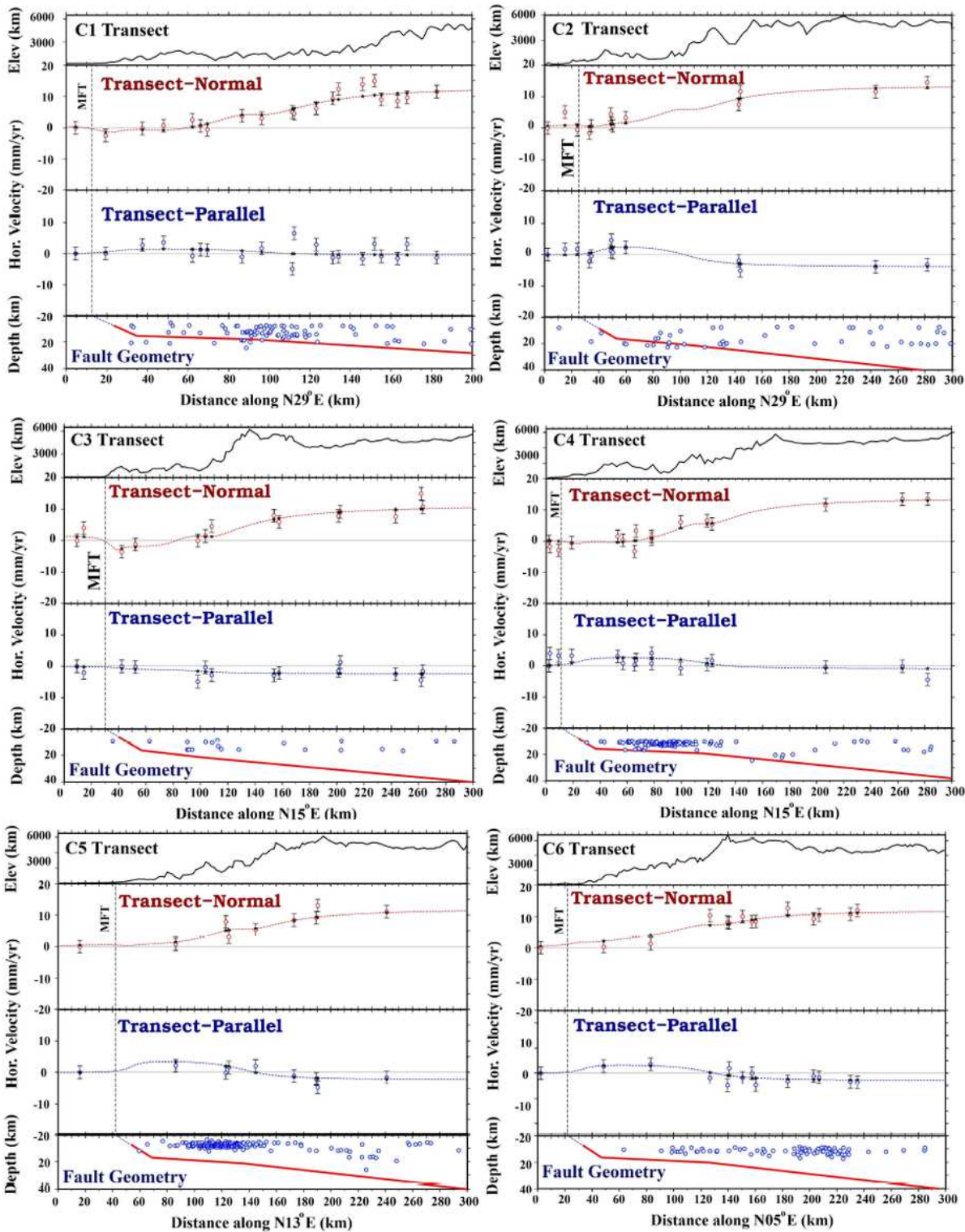


Figure 3

Modeling results across six profiles. The uppermost panel shows elevation of the topography (in meters) along the profiles. The two middle panels represent transect-normal and transect-parallel components of the horizontal velocity. The last panel indicates geometries of the faults. Light red and light blue circles with error bars in the transect-normal and transect-parallel components are surface velocities, whereas black stars are the modeled velocities. The red and blue dashed lines indicate the model fitting.

vertical black dashed lines denote surface locations of the fault. In the fault geometry panel, the dotted blue lines indicate fault locking and blue circles show observed seismicity ($M > 3.0$). MFT: Main Frontal Thrust.

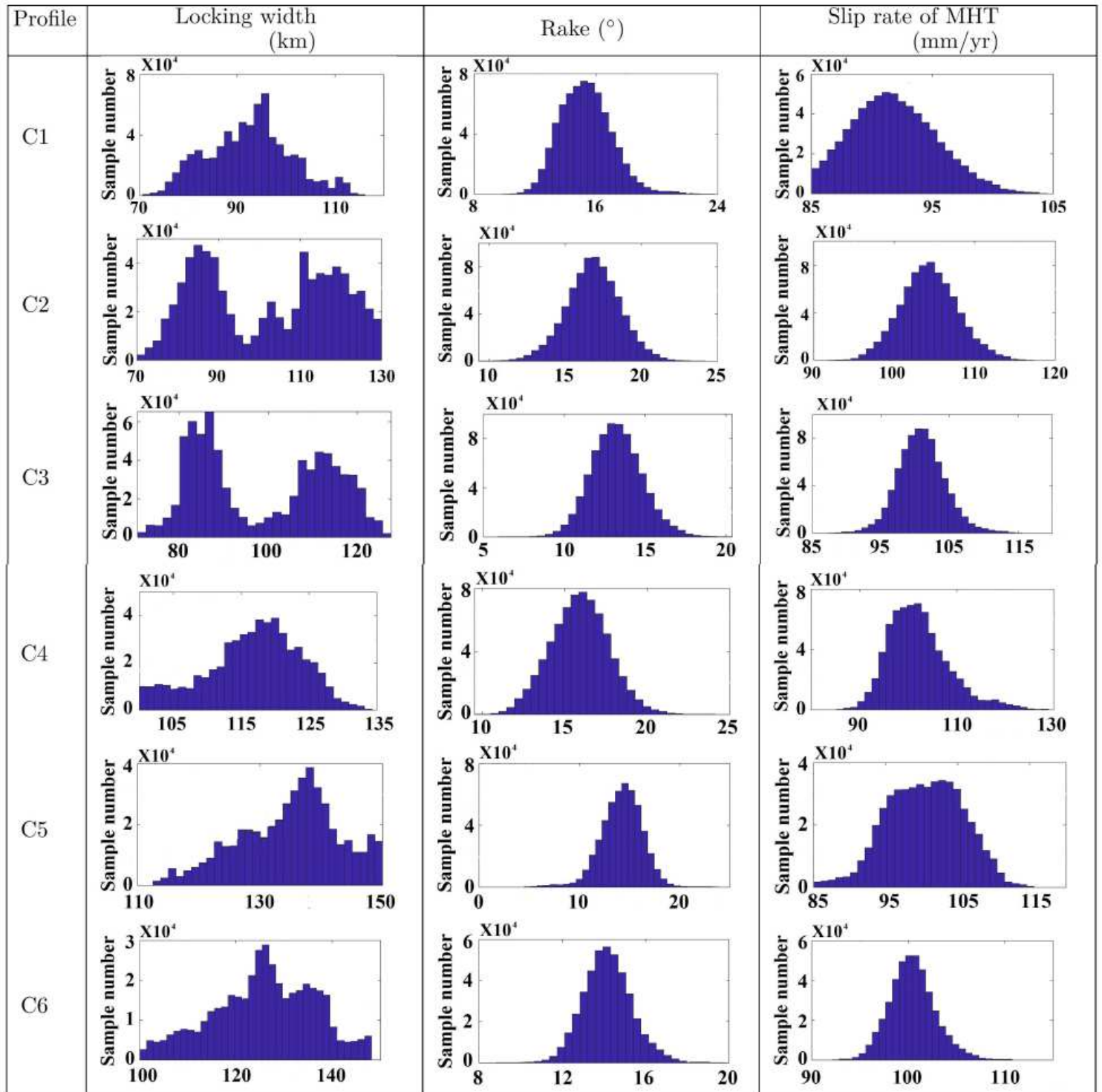


Figure 4

Posterior probability distribution of the model parameters.

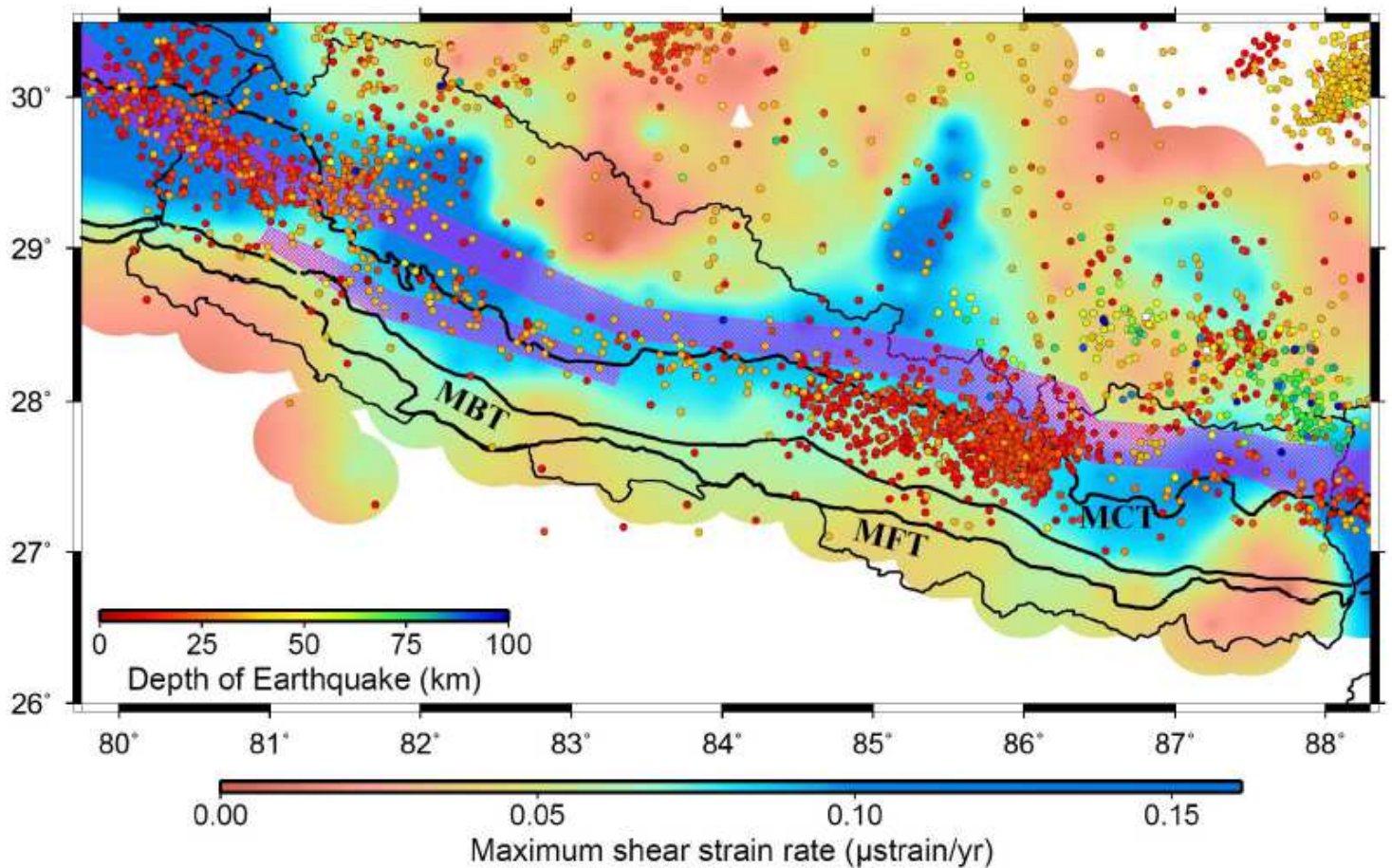


Figure 5

Maximum shear strain rate field along the central Himalaya. Small colored circles indicate background seismicity. The red shaded bands represent locking lines with one sigma uncertainties. MCT: Main Central Thrust, MBT: Main Boundary Thrust, MFT: Main Frontal Thrust Note: The designations employed and the presentation of the material on this map do not imply the expression of any opinion whatsoever on the part of Research Square concerning the legal status of any country, territory, city or area or of its authorities, or concerning the delimitation of its frontiers or boundaries. This map has been provided by the authors.

Supplementary Files

This is a list of supplementary files associated with this preprint. Click to download.

- [Supplementary.pdf](#)